Search for sub-eV scalar and pseudoscalar resonances via four-wave mixing with a laser collider

Hasebe, Takashi; Homma, Kensuke; Nakamiya, Yoshihide; Matsuura, Kayo; Otani, Kazuto; Hashida, Masaki; Inoue, Shunsuke; Sakabe, Shuji

PTEP
Prog. Theor. Exp. Phys. **2015**, 073C01 (19 pages)
DOI: 10.1093/ptep/ptv101

Search for sub-eV scalar and pseudoscalar resonances via four-wave mixing with a laser collider

Takashi Hasebe[1], Kensuke Homma[1,2,*], Yoshihide Nakamiya[3], Kayo Matsuura[1], Kazuto Otani[4], Masaki Hashida[3,5], Shunsuke Inoue[3,5], and Shuji Sakabe[3,5]

[1]*Graduate School of Science, Hiroshima University, Kagamiyama, Higashi-Hiroshima, Hiroshima 739-8526, Japan*
[2]*International Center for Zetta-Exawatt Science and Technology, Ecole Polytechnique, Route de Saclay, Palaiseau, F-91128, France*
[3]*Institute for Chemical Research, Kyoto University Uji, Kyoto 611-0011, Japan*
[4]*Institut national de la recherche scientifique–Energie Materiaux Telecommunications, 1650 Boulevard Lionel-Boulet, C.P.1020, Varennes (Quebec) J3X 1S2, Canada*
[5]*Graduate School of Science, Kyoto University, Sakyouku, Kyoto 606-8502, Japan*
*E-mail: homma@hepl.hiroshima-u.ac.jp

Received February 4, 2015; Revised June 12, 2015; Accepted June 17, 2015; Published July 28, 2015

Quasi-parallel photon–photon scattering by combining two-color laser fields is an approach to producing resonant states of low-mass fields in the laboratory. In this system resonances can be probed via the four-wave mixing process in the vacuum. A search for scalar and pseudoscalar fields was performed by combining a 9.3 μJ/0.9 ps Ti-sapphire laser and a 100 μJ/9 ns Nd:YAG laser. No significant signal of four-wave mixing was observed. We provide the upper limits on the coupling–mass relation for scalar and pseudoscalar fields, respectively, at a 95% confidence level in the mass region below 0.15 eV.

Subject Index C15, C19, C23, C33, C41

1. Introduction

Uncovering the nature of dark energy and dark matter is one of the most crucial problems in modern physics. Low-mass and weakly coupling fields predicted by theoretical models in cosmology and particle physics can be candidates for such dark components. For instance, based on the scalar–tensor theory with the cosmological constant Λ (STTΛ) [1], dark energy is interpreted as decaying Λ while the universe becomes older due to the gravitational coupling between extremely light dilatons, a kind of scalar field (ϕ), and matter fields. Observing the $\gamma\gamma \to \phi \to \gamma\gamma$ process with extremely high intensity laser fields can be a method of searching for ϕ in the laboratory [2]. The same approach can also be applied to searches for low-mass pseudoscalar fields (σ), if the photon spin states are properly chosen [3]. The axion [4,5], a pseudoscalar field associated with the breaking of Peccei–Quinn symmetry [6], is a suitable candidate to which this method is directly applicable. The axion is supposed to be one of the most reasonable candidates for cold dark matter [7,8]. Therefore, these theoretical models strongly motivate us to search for such fields in the laboratory in general.

Axion searches via two-photon coupling processes have been performed by a number of experiments, for example, solar axion searches [9–15], light shining through a wall [16–19], and the axion

Funded by SCOAP[3]

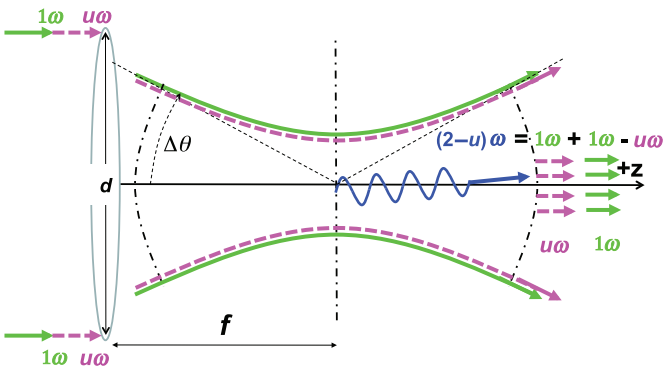

Fig. 1. Quasi-parallel colliding system by combining two-color laser fields [2], where d is the beam diameter, f the focal length, and the incident angle ϑ takes $0 < \vartheta \leq \Delta\theta$, which is unavoidable due to the ambiguity of the wave vectors of incident photons by the nature of focused lasers.

dark matter experiment [20,21]. Following the first search for scalar fields at a quasi-parallel colliding system (QPS) [22], the upgraded search for sub-eV scalar and pseudoscalar fields is presented in this paper.

With the schematic view of QPS in Fig. 1, we briefly explain the essence of our method as follows. By using variables defined at QPS, the center of mass system (CMS) energy between a randomly selected photon pair is expressed as

$$E_{\mathrm{CMS}} = 2\omega \sin\vartheta, \tag{1}$$

where ω is the energy of incident photons and ϑ is half of the incident angle of the photon pair. Extremely low collision energies are realizable at QPS by focusing a laser field because small values of ϑ can be automatically introduced.

In order to overcome low scattering amplitudes of $\gamma\gamma \to \phi/\sigma \to \gamma\gamma$ processes due to weak coupling, we first utilize the character of the integrated resonance effect by capturing E_{CMS} within ΔE_{CMS} via $\Delta\theta$ prepared by a creation laser field. Secondly, we let another laser field propagate into the optical axis common to the creation laser. This laser induces decay of resonance states into a specific energy–momentum space by the coherent nature of the inducing field. The scattering probability is thus proportionally increased by the number of photons in the inducing laser field [2,3,23,24].

The energies of decayed photons are defined by the energy conservation

$$\omega + \omega = (2-u)\,\omega + u\omega, \tag{2}$$

where u is an arbitrary number which satisfies $0 < u < 1$. We redefine the energies of final state photons as

$$\begin{aligned} \omega_3 &\equiv (2-u)\,\omega, \\ \omega_4 &\equiv u\omega, \end{aligned} \tag{3}$$

where ω_3 and ω_4 are the energies of the signal photon and inducing photons, respectively.

In the case of the scalar field exchange, the relation of linear polarization states between initial and final state photons when the wave vectors are on the same reaction plane are expressed as follows:

$$\begin{aligned} \omega\{1\} + \omega\{1\} &= \omega_3\{1\} + \omega_4\{1\}, \\ \omega\{1\} + \omega\{1\} &= \omega_3\{2\} + \omega_4\{2\}, \end{aligned} \tag{4}$$

where $\{1\}$ and $\{2\}$ are linear polarization states orthogonal to each other. In the pseudoscalar field exchange, the polarization relations are expressed as

$$\omega\{1\} + \omega\{2\} = \omega_3\{1\} + \omega_4\{2\},$$
$$\omega\{1\} + \omega\{2\} = \omega_3\{2\} + \omega_4\{1\}. \tag{5}$$

We emphasize that the above relations are limited only to the theoretically ideal case where all four photons are on the same reaction plane within the treatment based on plane waves. In the focused QPS, however, we must accept independent rotations of the incident p_1–p_2 plane and the outgoing p_3–p_4 plane as illustrated in Fig. A1 with respect to an experimentally given linear polarization plane. This implies that even if we supply ω as the pure $\{1\}$-state by a polarizer at the moment of plane wave propagation in advance of focusing, mixing of $\{1\}$ and $\{2\}$ states for randomly selected incident photon pairs is unavoidable while lasers are focused. Therefore, the focused QPS with a fixed initial linear polarization plane has sensitivity to both scalar and pseudoscalar fields simultaneously. We discuss this nature in detail in Appendix A.

The relation in Eq. (2) is similar to "four-wave mixing" in matter corresponding to the third-order nonlinear quantum optical process in atoms [25,26]. Therefore, the observation of the four-wave mixing process in the vacuum may be interpreted as a replacement of the atomic nonlinear process by the exchange of unknown scalar or pseudoscalar fields. The observation of four-wave mixing in the vacuum is also used as a method for testing higher-order QED effects [27–30].

Photons produced via the atomic four-wave mixing process can be the main background source for this search. The first search for scalar fields at QPS [22] was performed with weak intensity lasers, and thus the effect of the four-wave mixing process in atoms was negligible. In this experiment, however, four-wave mixing photons originating from the residual gas are anticipated due to much higher beam intensities. In this paper the method to obtain the exclusion limits in the search at QPS sensitive to both scalar and pseudoscalar fields is provided under the circumstance where a finite number of background photons must be evaluated.

2. The coupling–mass relation

The effective interaction Lagrangians coupling between two photons and ϕ/σ are expressed as

$$-L_\phi = gM^{-1}\tfrac{1}{4}F_{\mu\nu}F^{\mu\nu}\phi, \quad -L_\sigma = gM^{-1}\tfrac{1}{4}F_{\mu\nu}\tilde{F}^{\mu\nu}\sigma, \tag{6}$$

where M has the dimension of energy and g is a dimensionless constant. The yield of signal photons, $\mathcal{Y}$, is expressed with experimental parameters relevant to lasers and optical elements as follows:

$$\mathcal{Y} = \frac{1}{64\sqrt{2}\pi^4}\left(\frac{\lambda_c}{c\tau_c}\right)\left(\frac{\tau_c}{\tau_i}\right)\left(\frac{f}{d}\right)^3 \tan^{-1}\left(\frac{\pi d^2}{4f\lambda_c}\right)\frac{(\bar{u}-\underline{u})^2}{\bar{u}\underline{u}}$$
$$\times\left(\frac{gm\,[\mathrm{eV}]}{M\,[\mathrm{eV}]}\right)^2\left(\frac{m\,[\mathrm{eV}]}{\omega\,[\mathrm{eV}]}\right)^3 \mathcal{W}\mathcal{G}\mathcal{F}_s C_{mb}{N_c}^2 N_i, \tag{7}$$

where the subscripts c and i indicate the creation and inducing laser, respectively, λ is the wavelength, τ is the pulse duration, f is the focal length, d is the beam diameter, $\bar{u}$ and $\underline{u}$ are the upper and lower values on u determined by the spectrum width of ω_4, respectively, m is the mass of the exchanging field, $\mathcal{W}$ is the numerical factor relevant to the integral of the weighted resonance function which is refined in Eq. (B21) in Appendix B compared to $\mathcal{W} \sim \pi/2$ in Ref. [22], $\mathcal{G}$ is the incident plane rotation factor described in Appendix A, $\mathcal{F}_S$ is the polarization-dependent axially asymmetric

factor for outgoing photons [3], C_{mb} is the combinatorial factor originating from selecting a pair of photons among multimode frequency states, and the N are the average numbers of photons in the coherent state. The detail of the formulation of the signal yield is summarized in the Appendix of Ref. [22]. The coupling constant g/M is expressed as

$$\frac{g}{M\,[\mathrm{eV}]} = 2^{1/4}8\pi^2 \sqrt{\frac{\mathcal{Y}\omega^3\,[\mathrm{eV}]}{\left(\frac{\lambda_c}{c\tau_c}\right)\left(\frac{\tau_c}{\tau_i}\right)\left(\frac{f}{d}\right)^3 \tan^{-1}\left(\frac{\pi d^2}{4f\lambda_c}\right)\frac{(\bar{u}-\underline{u})^2}{\bar{u}\underline{u}}\mathcal{W}\mathcal{G}\mathcal{F}_s C_{mb}{N_c}^2 N_i}} m^{-5/2}\,[\mathrm{eV}]. \quad (8)$$

3. Experimental setup

We explain the experimental setup to detect signals of four-wave mixing in the vacuum. The schematic view of the setup is shown in Fig. 2.

A Ti-sapphire laser (wavelength 800 nm) and a Nd:YAG laser (wavelength 1064 nm) are used as the creation and inducing lasers, respectively. To reduce the number of background photons emitted from the residual gas via four-wave mixing, the linear polarization states of the creation and inducing lasers are configured to linear polarization states $\{1\}$ and $\{2\}$, respectively. The beam alignments of the lasers are monitored by CCD cameras (CCD) and the pulse energies of the creation and inducing lasers are measured by photodiodes (PD). These beams are combined by a dichroic mirror (DM). The combined beams are guided into the vacuum chamber at the 20 mm beam diameter and focused with the convex lens at the focal length of 200 mm.

The expected wavelength of the corresponding signal photon is evaluated from the following equation:

$$\lambda_s = \frac{\lambda_i\lambda_c/2}{\lambda_i - \lambda_c/2} = 641\,\mathrm{nm}. \quad (9)$$

A light source with a central wavelength of 640 nm is combined with the creation and inducing lasers by DM to evaluate the detection efficiency and to trace the trajectory of signal photons for the detector alignment.

The agreement of the optical axes between the two lasers is adjusted at a precision of 2–3 μm by monitoring individual beam profiles at the near side and the far side of the focal spot with the CCD camera. The beam profiles at the focal spot are shown in Fig. 3. The spot sizes of the creation and inducing lasers, which are defined as $2\,\sigma$ of the 2D Gauss functions fitting the beam profiles, are 21 μm and 23 μm, respectively. The creation laser overlaps with 87% of the beam energy of the inducing laser at the focal spot. Thus, the effective beam energy of the inducing laser is evaluated by correcting the measured beam energy with this overlapping factor.

Signal photons generated within the focal volume travel along the common optical axis of the combined lasers. Signal photons are separated from the creation and inducing lasers by the prism, and signal wave filters are placed to further eliminate the residual photons from the combined lasers. The polarization beam splitter (PBS) transmits $\{1\}$-polarized photons and reflects $\{2\}$-polarized photons. Incident photons are split between the shorter optical fiber Path$\{1\}$ and the longer Path$\{2\}$. The incident photons to PBS are eventually observed by the common photo-device having relative time delay

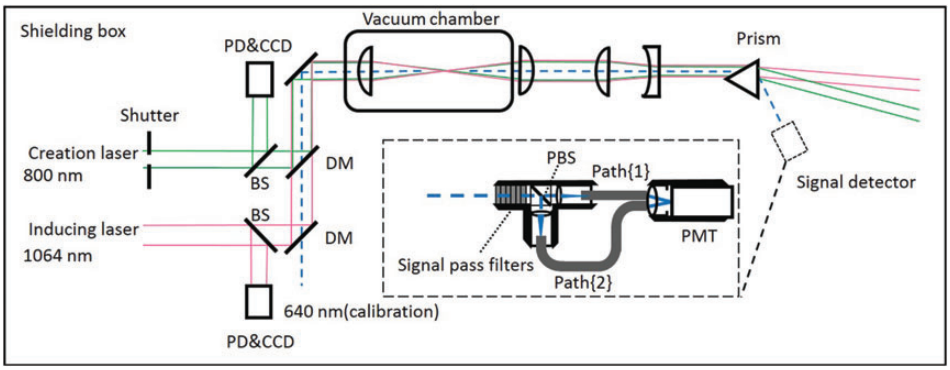

Fig. 2. Schematic view of the experimental setup.

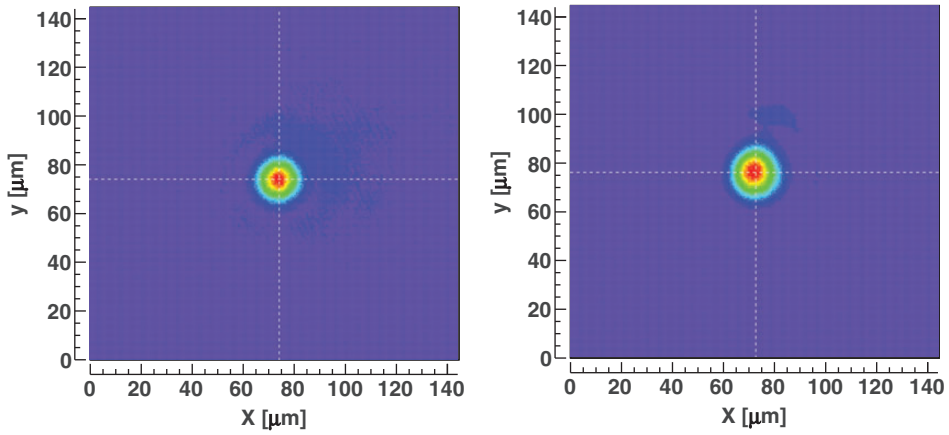

Fig. 3. The beam profiles of the creation laser (left) and the inducing laser (right) at the common focal point captured by a common CCD camera.

of 23 ns. We use a single-photon-countable photomultiplier tube (PMT; R7400-01, manufactured by HAMAMATSU) as the photo-device.

The repetition rate of the creation laser is 1 kHz and that of the inducing laser is 10 Hz by synchronizing the trigger with the 1 kHz creation pulsing. The data acquisition trigger of 20 Hz is synchronized with the 1 kHz creation laser pulsing which includes pedestal triggers in order to provide four patterns of triggers. The time coincidence between creation and inducing pulses is performed by adjusting the relative injection timing between the two lasers so that the relative time maximizes the four-wave mixing yield in the air. The shutter is placed on the creation laser beam line and it repeatedly opens and closes every 5 seconds. We acquire data with the four patterns of triggers, which are "both lasers are incident (S)," "only the creation laser is incident (C)," "only the inducing laser is incident (I)," and "neither laser is incident (P)." The digital oscilloscope recorded waveform data from the PMT and two photodiodes synchronized with the 20 Hz data acquisition trigger. The recorded waveform data from the PMT are sorted into the four types of trigger pattern: S, C, I, and P. The four trigger patterns are classified by checking the charge correlations between the waveform data from the two photodiodes for intensity monitoring.

4. Method of waveform analysis

The observed photon counts are estimated by analyzing the waveform data from the PMT. The individual waveform consists of 500 sampling data points within a 200 ns time window. We search

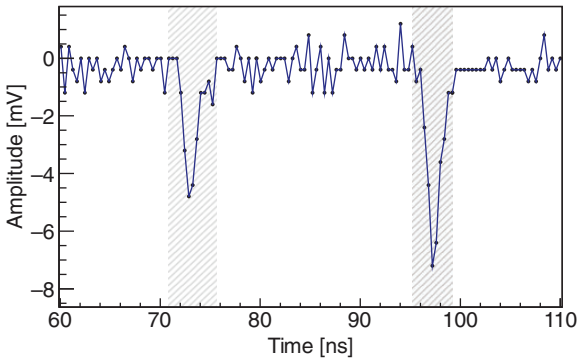

Fig. 4. A waveform data sample with two peak structures. The black shaded areas show the integral ranges to evaluate the charge sums of individual peak structures.

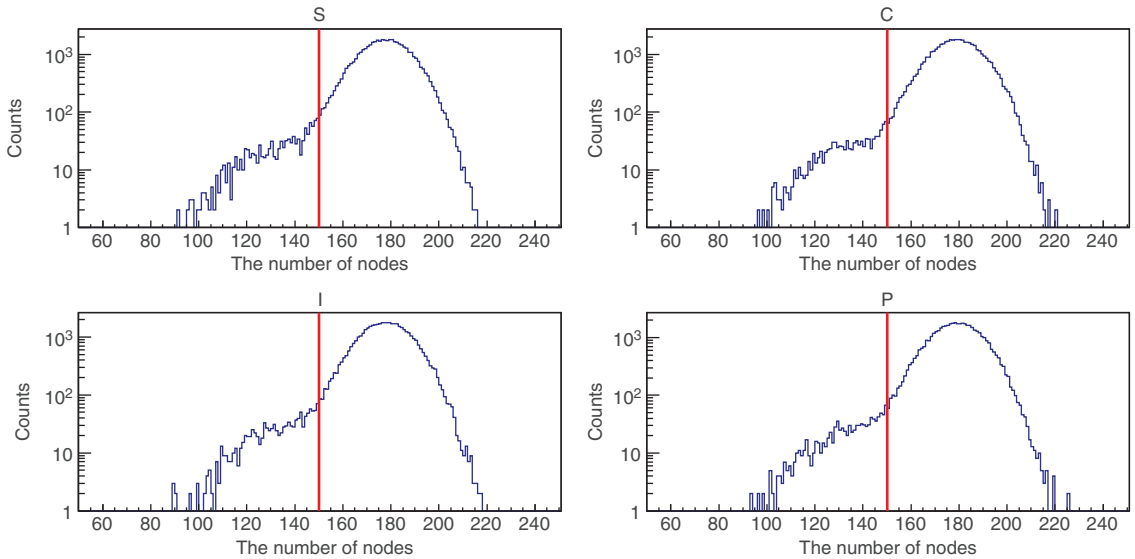

Fig. 5. Distributions of the number of nodes for trigger patterns S, C, I, and P. The events with fewer numbers of nodes below the red vertical line are identified as noisy events.

for negative peaks whose amplitude exceeds a given threshold. We then calculate charge sums of the peak structures. Figure 4 shows a sample of waveform data where peak structures are identified. Charge sums of peak structures are evaluated in units of the single-photon equivalent charge, -4.21×10^{-14} C.

There are some accidental noisy events among the recorded waveform data. In our analysis method, these noise structures could be misidentified as large photon-like peak structures. Therefore, it is necessary to remove such noisy events from the analyzed waveform data before counting photon-like peaks. We can identify noisy events by analyzing the frequencies of the waveforms. Noisy waveforms tend to have lower frequencies than those of normal waveforms. The frequencies are estimated by counting the number of nodes, which is defined as the intersections between a waveform and the average line of amplitudes within the 200 ns time window. The distributions of the number of nodes for each trigger pattern are shown in Fig. 5. We regard a waveform of which the number of nodes is lower than 150 as a noisy event in all trigger patterns by confirming that the differences of the distributions among four trigger patterns are not prominent. Typical waveforms of noisy events and normal events identified by this method are shown in Fig. 6.

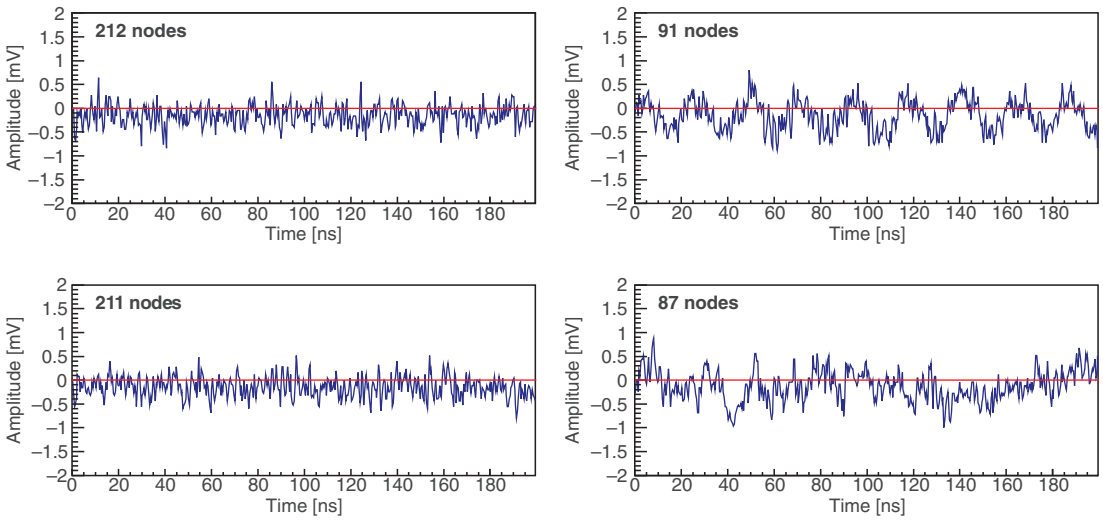

Fig. 6. Examples of waveforms of noisy events and normal events. The two panels on the left and right sides show waveforms of normal events and noisy events, respectively. The red horizontal lines indicate the averages of the amplitudes of sampling points for each waveform.

5. Measurement of the four-wave mixing process in the residual gas

Background photons can be produced via the four-wave mixing process occurring in residual atoms in the vacuum chamber. To estimate the expected number of background photons, we measured the pressure dependence of the number of four-wave mixing photons in gas. Figure 7 shows arrival time distributions of observed photons in the air at 5.0×10^4 Pa among four trigger patterns. Specific two-peak structures appear only for the S pattern. These peak structures have approximately a 23 ns time interval, which agrees with the optical path length difference between Path$\{1\}$ and Path$\{2\}$. We count the number of photons within a time domain $T\{1\}$ (71–75 ns) for the $\{1\}$-polarized state and $T\{2\}$ (94–98 ns) for the $\{2\}$-polarized state.

The number of four-wave mixing signals N_S are evaluated from the following equation (see Eqs. (18) and (19) in Ref. [22]):

$$N_{\mathrm{S}} = n_{\mathrm{S}} - \frac{W_{\mathrm{S}}}{W_{\mathrm{C}}} n_{\mathrm{C}} - \frac{W_{\mathrm{S}}}{W_{\mathrm{I}}} n_{\mathrm{I}} + \frac{W_{\mathrm{S}}}{W_{\mathrm{P}}} n_{\mathrm{P}}, \tag{10}$$

where n_i and W_i denote the number of photon-like peaks in the signal domains and the number of events in trigger pattern i, respectively.

The pressure dependence of the number of four-wave mixing photons per S-trigger event are shown in Fig. 8. Data points are fit by the quadratic function of pressure. We extrapolate the number of four-wave mixing photons in the residual gas at 2.3×10^{-2} Pa (an equivalent condition to the vacuum data we discuss later) from the fitting function. The efficiency-corrected number of $\{1\}$-polarized and $\{2\}$-polarized photons in residual gas $\mathcal{N}_{\mathrm{gas1}}$ and $\mathcal{N}_{\mathrm{gas2}}$ with the same shot statistics as the vacuum data are evaluated as follows:

$$\begin{aligned} \mathcal{N}_{\mathrm{gas1}} &= 1.7 \pm 1.1 \times 10^{-5}, \\ \mathcal{N}_{\mathrm{gas2}} &= 1.7 \pm 1.1 \times 10^{-5}. \end{aligned} \tag{11}$$

We confirmed that the expected value of four-wave mixing photons from the residual gas is negligibly small in the vacuum data for a given total statistics.

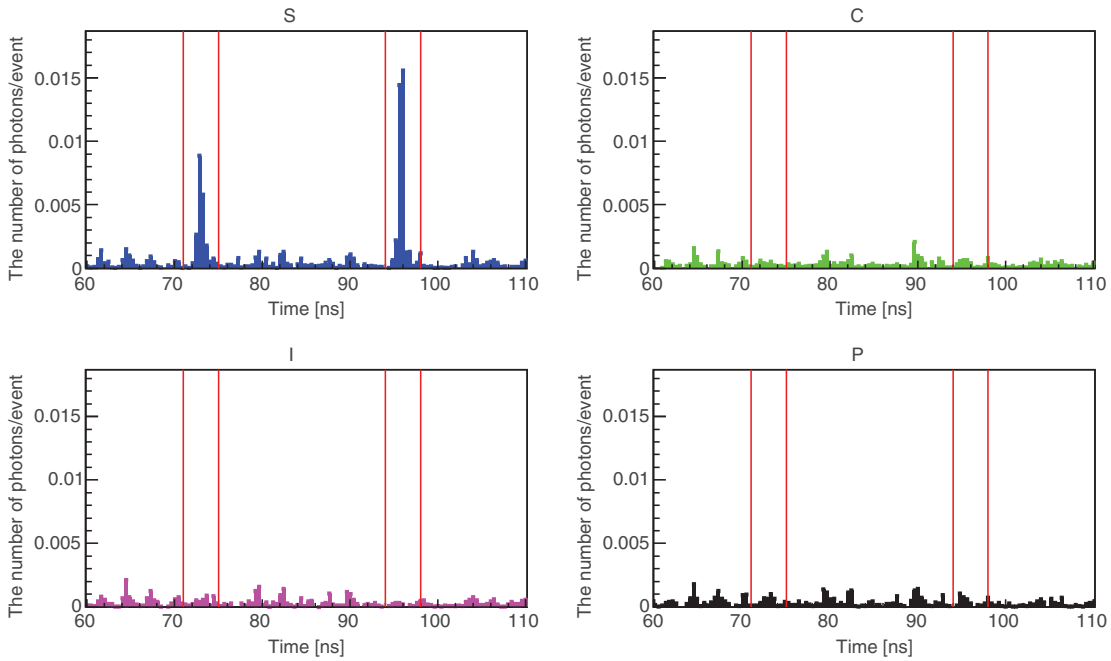

Fig. 7. The arrival time distributions of observed photons per triggered event (efficiency-uncorrected) at 5.0×10^4 Pa. The left and right bands bounded by two neighboring red lines in each panel indicate the time domains $T\{1\}$ and $T\{2\}$ where $\{1\}$- and $\{2\}$-polarized photons are expected to be observed, respectively. In this figure, the threshold value for peak identification is set lower than that of the actual data analysis on purpose to show typical pedestal structures in each trigger pattern.

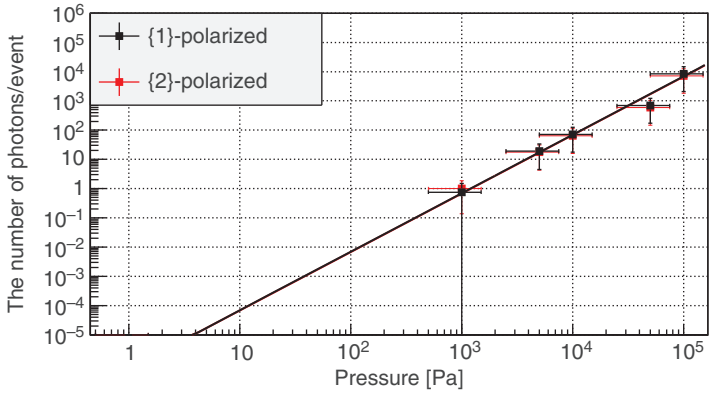

Fig. 8. The pressure dependence of the number of four-wave mixing photons in the residual gas inside the interaction chamber per S-trigger event. The red and black lines represent the fitting functions for the $\{1\}$- and $\{2\}$-polarized states, respectively.

6. The search for four-wave mixing signals in the vacuum

We acquired data at 2.3×10^{-2} Pa in the search for the resonant states of the ϕ and σ fields. Figure 9 shows the arrival time distributions of observed photon counts. Table 1 summarizes the numbers of observed photon-like signals evaluated in units of the single-photon equivalent charge with $\{1\}$- and $\{2\}$-polarized states for each trigger pattern, respectively.

After performing subtractions between the four patterns of the histograms in Fig. 9 based on the relation in Eq. (10), we obtained the time distribution of N_S as shown in Fig. 10. The numbers of

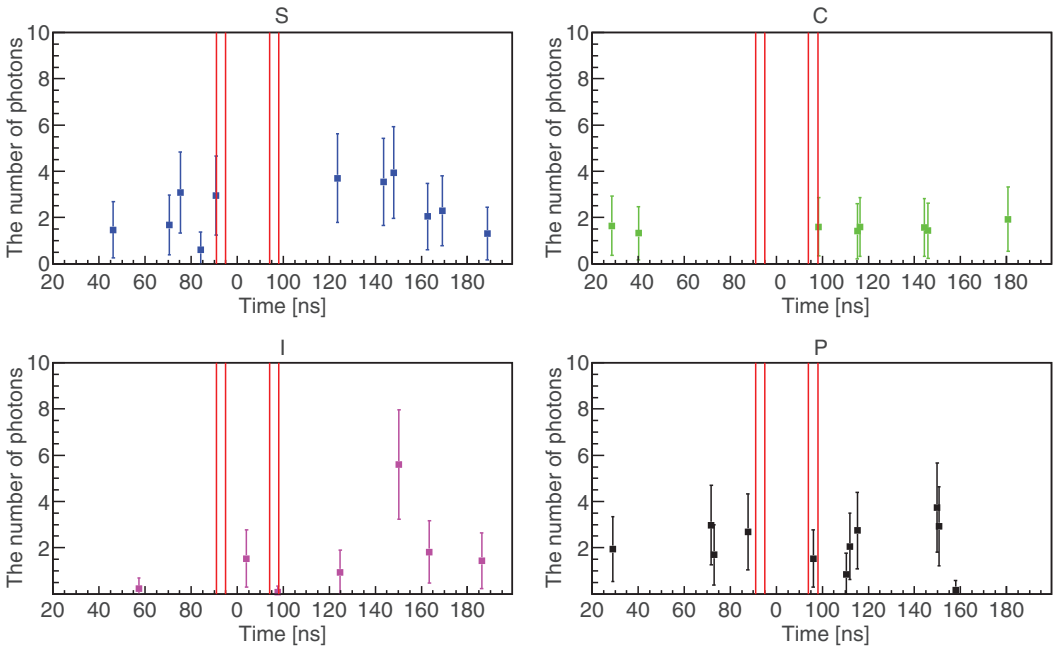

Fig. 9. Arrival time distributions of observed photons at 2.3×10^{-2} Pa. The data points in each trigger pattern are normalized to the number of triggered events of the S trigger pattern.

Table 1. The numbers of observed photons in $T\{1\}$ and $T\{2\}$ for each trigger pattern. n_{i1} and n_{i2} are the numbers of photons evaluated in units of single-photon equivalent charge in trigger pattern i with $\{1\}$- and $\{2\}$-polarized states, respectively. W_i is the number of events in trigger pattern i.

Trigger i	n_{i1}	n_{i2}	W_i
S	0	0	46120
C	0	0	46203
I	0	0.07	46044
P	0	1.53	46169

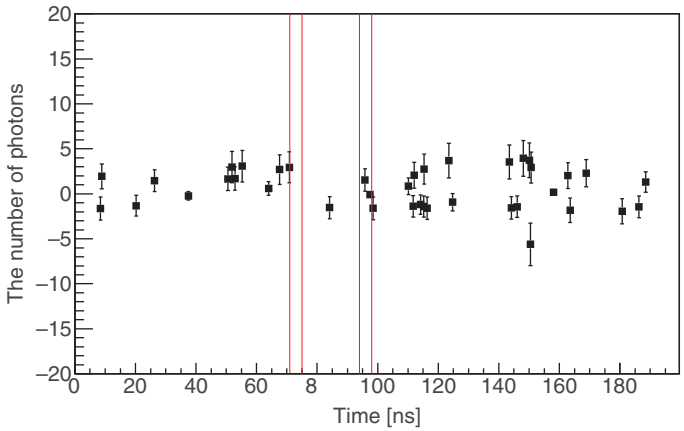

Fig. 10. The arrival time distribution of N_S defined in Eq. (10).

Table 2. Data table of experimental parameters. $\mathcal{G}^{\rm sc}_{11}$ and $\mathcal{G}^{\rm ps}_{12}$ represent the incident plane rotation factor for the scalar and pseudoscalar field exchanges, respectively. The evaluation of $\mathcal{G}$ is discussed in Appendix A. $\mathcal{F}^{\rm sc}_{1122}$ and $\mathcal{F}^{\rm ps}_{1212}$ denote the axially asymmetric factor for scalar and pseudoscalar field exchanges, respectively. See the detail in the Appendix of Ref. [3].

Parameters	Values
Center of wavelength of creation laser $\lambda_{\rm c}$	800 nm
Relative line width of creation laser $(\delta\omega/\langle\omega\rangle)$	7.5×10^{-3}
Center of wavelength of inducing laser $\lambda_{\rm i}$	1064 nm
Relative line width of inducing laser $(\delta\omega_4/\langle\omega_4\rangle)$	1.0×10^{-4}
Duration time of creation laser pulse per injection $\tau_{\rm c}$	900 fs
Duration time of inducing laser pulse per injection $\tau_{\rm i}$	9 ns
Creation laser energy per $\tau_{\rm c}$	$9.3 \pm 1.2\,\mu$J
Inducing laser energy per $\tau_{\rm i}$	$100 \pm 1\,\mu$J
Focal length f	200 mm
Beam diameter of laser beams d	20 mm
Upper mass range given by $\theta < \Delta\theta$	0.15 eV
$u = \omega_4/\omega$	0.75
Incident plane rotation factor $\mathcal{G}$	$\mathcal{G}^{\rm sc}_{11} = 19/32$
	$\mathcal{G}^{\rm ps}_{12} = 1/2$
Axially asymmetric factor $\mathcal{F}_s$	$\mathcal{F}^{\rm sc}_{1122} = 19.4$
	$\mathcal{F}^{\rm ps}_{1212} = 19.2$
Combinatorial factor in luminosity C_{mb}	1/2
Single-photon detection efficiency $\epsilon_{\rm D}$	1.4 ± 0.1 %
Efficiency of optical path from interaction point to Path$\{1\}$ $\epsilon_{\rm opt1}$	0.5 ± 0.1 %
Efficiency of optical path from interaction point to Path$\{2\}$ $\epsilon_{\rm opt2}$	0.9 ± 0.2 %
$\delta N_{\rm S1}$	2.2
$\delta N_{\rm S2}$	4.4

signals with $\{1\}$- and $\{2\}$-polarized states are, respectively, given as follows:

$$N_{\rm S1} = 0 \pm 0\ (\text{stat.}) \pm 2.16\ (\text{syst.I}) \pm 0.30\ (\text{syst.II}) \pm 0\ (\text{syst.III}),$$
$$N_{\rm S2} = 1.46 \pm 1.27\ (\text{stat.}) \pm 2.16\ (\text{syst.I}) \pm 0.04\ (\text{syst.II}) \pm 3.59\ (\text{syst.III}). \quad (12)$$

The systematic error I originates from the number of photons outside of the two arrival time windows for the $\{1\}$- and $\{2\}$-polarized states. This was evaluated by calculating the root mean square of $N_{\rm S}$, except in the $T\{1\}$ and $T\{2\}$ windows. The systematic error II originates from the dependence on the threshold values for the peak finding -1.3 ± 0.1 mV. The systematic error III is relevant to the ambiguities of the rejection of noisy events, 150 ± 5 nodes.

7. The excluded coupling–mass limits for scalar and pseudoscalar fields

There is no significant four-wave mixing signal in this search from the result in (12). We thus evaluate the exclusion regions on the coupling–mass relation as follows.

We estimate the upper limit on the sensitive mass range as

$$m < 2\omega \sin\Delta\theta \sim 2\omega\frac{d}{2f} = 0.15\,\text{eV} \quad (13)$$

based on the values summarized in Table 2, where ϑ in Fig. 1 varies from 0 to $\Delta\theta$ defined by a focal length f and a beam diameter d.

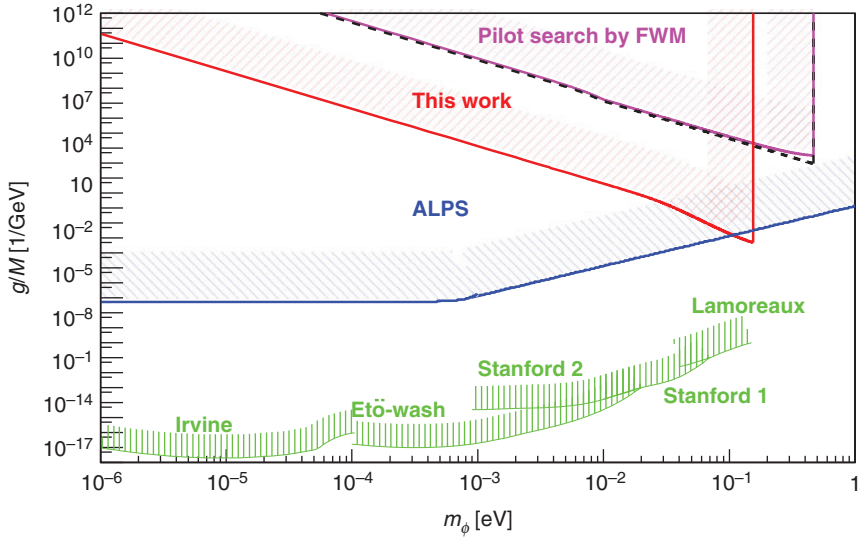

Fig. 11. Exclusion limits for scalar fields (ϕ) in ϕ–photon coupling (g/M) as a function of the mass of ϕ (m_ϕ). The region excluded by this experiment is shown by the red shaded area. The magenta shaded area shows the region excluded by our previous search, which is renewed from the black dotted line obtained from Ref. [22] by taking the incident plane rotation factor $\mathcal{G}$ and the mass-dependent $\mathcal{W}$ factor in Appendix B into account. The blue shaded area represents the region excluded for scalar fields by the light shining through a wall experiment "ALPS" [19] (for the mass region above 10^{-3} eV, the sine function part of the sensitivity curve is simplified to unity for drawing purposes). The green shaded areas indicate the limits given by non-Newtonian force searches by the torsion balance experiments "Irvine" [32], "Eto-wash" [33,34], "Stanford1" [35], "Stanford2" [36], and Casimir force measurement "Lamoreaux" [37].

The number of efficiency-corrected {1}-polarized signal photons $\mathcal{N}_{S1}$ and that of {2}-polarized signal photons $\mathcal{N}_{S2}$ are evaluated from the following relations with the experimental parameters:

$$\mathcal{N}_{S1} = \frac{N_{S1}}{\epsilon_{opt1}\epsilon_D}, \quad \mathcal{N}_{S2} = \frac{N_{S2}}{\epsilon_{opt2}\epsilon_D}, \tag{14}$$

where ϵ_{opt1} and ϵ_{opt2} are the attenuation ratios of the signal photons propagating from the interaction point through Path{1} and Path{2}, respectively.

These attenuation factors are composed of the transmittance of optical devices and the acceptance of signal paths with respect to the actual location of the PMT. They are inclusively evaluated by sampling the beam energies of the 640 nm calibration light at the focal point and the detection point, respectively, and taking the ratio between them. The matching of beam paths between the calibration light and four-wave mixing signals is ensured by adjusting the beam center of the calibration light with respect to those of the creation and inducing lasers at the near side and the far side of the focal spot, respectively. ϵ_D is the signal detection efficiency of the PMT mainly caused by the quantum efficiency of the device. ϵ_D is evaluated using a 532 nm pulse laser in advance of the search. We evaluate the absolute detection efficiency by splitting the 532 nm beam equally and taking the ratio between these energies. One is measured by a calibrated beam energy meter and the other is measured by the PMT with neutral density filters with measured attenuation factors. We then corrected the difference of the quantum efficiencies between the 532 nm and 641 nm lights by taking the relative quantum efficiencies provided by HAMAMATSU into account.

We then evaluate upper limits on the coupling–mass relation at a 95% confidence level on the basis that the fluctuation of the number of signal yields forms a Gaussian distribution. We define δN_S as the one standard deviation of N_S. It is evaluated from the quadratic sum of statistical and systematic

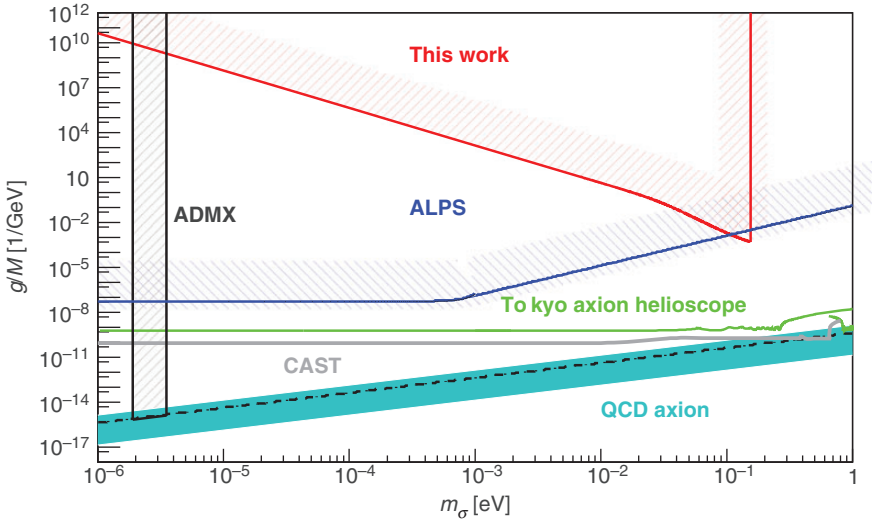

Fig. 12. Exclusion limits for pseudoscalar fields (σ) in σ–photon coupling (g/M) as a function of the mass of σ (m_σ). The blue shaded area shows the region excluded by the pseudoscalar search, "ALPS." The green and gray solid lines show the exclusion limits from the solar axion experiments "Tokyo Axion Helioscope" [9–11] and "CAST" [13–15], respectively. The black shaded area represents the result from the dark matter axion search using a microwave cavity "ADMX" [20,21]. The cyan band indicates the expected coupling–mass relation of the QCD axion predicted by the KSVZ model [38,39] with $|E/N - 1.95|$ in the range 0.07–7; furthermore, the case of $E/N = 0$ is shown by the black dotted line.

errors in Eq. (12), and $2.24\delta N_{\rm S}$ is the upper limit of $N_{\rm S}$ when we obtain a 95% confidence level (see Eq. (36.56) in Ref. [31]). The upper limit of signal yields per shot $\mathcal{Y}_{\rm sc}$ (for the scalar field exchange) and $\mathcal{Y}_{\rm ps}$ (for the pseudoscalar field exchange) are evaluated as follows:

$$\mathcal{Y}_{\rm sc} = \frac{2.24\delta N_{\rm S2}}{\epsilon_{\rm opt2}\epsilon_{\rm D} W_{\rm S}}, \qquad \mathcal{Y}_{\rm ps} = \frac{2.24\delta N_{\rm S1}}{\epsilon_{\rm opt1}\epsilon_{\rm D} W_{\rm S}}. \tag{15}$$

As we briefly mention in Sect. 1 and in detail in Appendix A, even though we fix the linear polarization planes for the creation and inducing laser fields by the polarizers at the moment of plane wave propagation, mixing of {1}- and {2}-polarization states is unavoidable in the focused QPS. By this effect, the focused system has sensitivity to both scalar and pseudoscalar fields simultaneously.

We obtain the coupling–mass relation from Eq. (8). The exclusion limits for scalar and pseudoscalar fields at a 95% confidence level are shown in Figs. 11 and 12, respectively.

8. Conclusions

A search for scalar and pseudoscalar fields via the four-wave mixing precess at QPS has been performed by focusing 10 μJ/0.9 ps and 100 μJ/9 ns pulse lasers. The number of {1}- and {2}-polarized signal-like photons are $N_{\rm S1} = 0 \pm 0$ (stat.) ± 2.16 (syst.I) ± 0.30 (syst.II) ± 0 (syst.III) and $N_{\rm S2} = 1.46 \pm 1.27$ (stat.) ± 2.16 (syst.I) ± 0.04 (syst.II) ± 3.59 (syst.III), respectively. We confirmed that the expected number of four-wave mixing photons in the residual gas is negligibly small by measuring the pressure dependence. As a result, no significant four-wave mixing signal is observed in this experiment. We obtained the upper limits on the coupling–mass relation for scalar and pseudoscalar fields at a 95% confidence level, respectively. The most sensitive coupling limits $g/M = 5.24 \times 10^{-4}\,{\rm GeV}^{-1}$ for scalar search and $g/M = 5.42 \times 10^{-4}\,{\rm GeV}^{-1}$ for pseudoscalar search are obtained at $m = 0.15$ eV.

Acknowledgements

We gratefully thank S. Tokita and Y. Miyasaka for operation and maintenance of laser systems. We appreciate Y. Inoue providing the data list of the sensitive curve for the Tokyo axion helioscope.

K. Homma, as the corresponding author, cordially thanks Y. Fujii for the detailed discussions and careful checks with him on the polarization dependence of the scattering probability. He expresses his gratitude to T. Tajima and G. Mourou for many aspects relevant to this subject. He finally acknowledges the strong financial supports by Grants-in-Aid for Scientific Research nos. 24654069, 25287060, and 26104709 from MEXT of Japan, the Collaborative Research Program of the Institute for Chemical Research, Kyoto University (grants No. 2012-6, No. 2013-56, and No. 2014-72), and the MATSUO FOUNDATION.

Funding

Open Access funding: SCOAP[3].

Appendix A. Evaluation of the incident plane rotation factor $\mathcal{G}$

Figure A1 illustrates the relation between the experimentally defined linear polarization directions $\{1\}$ and $\{2\}$ and those theoretically defined (1) and (2). It also depicts the relations between the p_1–p_2 and p_3–p_4 planes with respect to the x–z plane, where the theoretically allowed coupling of an exchanged field to the linear polarization states can be evaluated in the clearest way. In Ref. [3], we have assumed the incident photons p_1 and p_2 are both plane waves with different wave vectors on the same reaction plane, which always ensures the clearest condition. In the general three-dimensional incident case such as a focused Gaussian beam, however, the p_1–p_2 plane can rotate with respect to the x–z plane, which results in a deviation from the theoretically clearest condition. We therefore introduce a weighted averaging factor $\mathcal{G}$ over the clockwise rotation angle Φ of the incident reaction plane with respect to the x-axis as follows.

As discussed in Ref. [3], the Lorentz invariant s-channel scattering amplitude for the Lagrangian defined in Eq. (6) has the following basic form:

$$\mathcal{M}_S = -\left(gM^{-1}\right)^2 \frac{\mathcal{V}_{ab}^{[1]}\mathcal{V}_{cd}^{[2]}}{(p_1+p_2)^2+m^2}, \tag{A1}$$

where $S \equiv abcd$ with $a, b, c, d = 1$ or 2, respectively, denotes a sequence of four-photon polarization states and m is the mass of the scalar or pseudoscalar field. With the vectors defined below, the vertex factors for the scalar case (SC) are expressed as

$$\begin{aligned}\mathcal{V}_{ab}^{[1]\mathrm{SC}} &= (p_1p_2)\left(e_1^{(a)}e_2^{(b)}\right) - \left(p_1e_2^{(a)}\right)\left(p_2e_1^{(b)}\right),\\ \mathcal{V}_{cd}^{[2]\mathrm{SC}} &= (p_3p_4)\left(e_3^{(c)}e_4^{(d)}\right) - \left(p_3e_4^{(c)}\right)\left(p_4e_3^{(d)}\right),\end{aligned} \tag{A2}$$

and those for the pseudoscalar case (PS) are expressed as

$$\begin{aligned}\mathcal{V}_{ab}^{[1]\mathrm{PS}} &= -\epsilon^{\mu\nu\rho\sigma}\,p_{1\mu}p_{2\rho}e_{1\nu}^{(a)}e_{2\sigma}^{(b)},\\ V_{cd}^{[2]\mathrm{PS}} &= -\epsilon^{\mu\nu\rho\sigma}\,p_{3\mu}p_{4\rho}e_{3\nu}^{(c)}e_{4\sigma}^{(d)}.\end{aligned} \tag{A3}$$

We must first take into account the clockwise rotation angle φ of the p_3–p_4 plane with respect to the given x–z plane independent of the p_1–p_2 plane, because these two planes are not coplanar in QPS, contrary to the situation where the coplanar condition of p_1 through p_4 is always satisfied

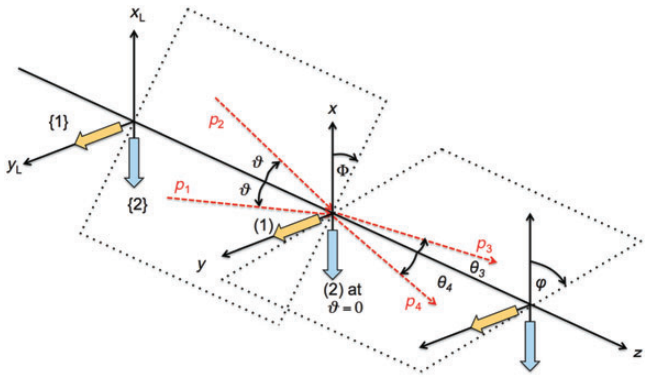

Fig. A1. Definitions of polarization vectors and rotation angles in QPS.

in CMS. This implies that the simple summation factor 2π on the azimuthal degree of freedom of the solid angle cannot be applied to QPS; instead, the φ-dependent squared transition amplitude must be summed over the possible rotation φ from 0 to 2π. We have already introduced this axially asymmetric factor $\mathcal{F}_S$ with respect only to the incident reaction plane at $\Phi = 0$ in [3]. This factor essentially depends only on the second vertex factors above, while the incident plane rotation factor $\mathcal{G}$ is relevant only to the first vertex factors. We thus define the incident plane rotation factor as a weighted average with respect to $\mathcal{F}_S$ at $\Phi = 0$ as follows:

$$\mathcal{G}_{ab} \equiv \frac{\int_0^{2\pi} \left| \mathcal{V}_{ab}^{[1]}(\Phi) \right|^2 d\Phi}{\int_0^{2\pi} \left| \mathcal{V}_{ab}^{[1]}(\Phi = 0) \right|^2 d\Phi}, \tag{A4}$$

because experiments cannot fix the incident reaction plane and the intensity of the creation laser field must be shared over the possible incident reaction planes.

By requiring (1)={1} and (2)={2} at $\Phi = \varphi = 0$ where the theoretically clearest polarization relations can interface with the experimental condition, we describe the polarization vectors and momentum vectors for four photons with rotation angles Φ and φ as follows:

$$\begin{aligned}
e_i^{(1)} &= (0, 1, 0)\,, && \text{(A5)}\\
e_1^{(2)} &= (-\cos\vartheta, 0, \sin\vartheta)\,, \quad e_2^{(2)} = (-\cos\vartheta, 0, -\sin\vartheta)\,,\\
e_3^{(2)} &= (-\cos\theta_3, 0, \sin\theta_3)\,, \quad e_4^{(2)} = (-\cos\theta_4, 0, -\sin\theta_4)\,,\\
p_1 &= (\omega\sin\vartheta\cos\Phi, -\omega\sin\vartheta\sin\Phi, \omega\cos\vartheta; \omega)\,,\\
p_2 &= (-\omega\sin\vartheta\cos\Phi, \omega\sin\vartheta\sin\Phi, \omega\cos\vartheta; \omega)\,,\\
p_3 &= (\omega_3\sin\theta_3\cos\varphi, -\omega_3\sin\theta_3\sin\varphi, \omega_3\cos\theta_3; \omega_3)\,,\\
p_4 &= (-\omega_4\sin\theta_4\cos\varphi, \omega_4\sin\theta_4\sin\varphi, \omega_4\cos\theta_4; \omega_4)\,. && \text{(A6)}
\end{aligned}$$

We note here that we cannot rotate polarization vectors because the experiment must introduce fixed polarization vectors. This implies that the clear distinction between scalar and pseudoscalar couplings cannot be stated due to non-zero rotation angles because non-identical linear polarization planes between photon 1 and 2 or photon 3 and 4 are implicitly introduced.

Based on these vectors, we summarize the relations between momenta and polarization vectors with photon labels $i = 1, 2, 3, 4$ as follows:

$$\left(p_1 e_j^{(1)}\right) = -\omega \sin\vartheta \sin\Phi, \quad \left(p_2 e_j^{(1)}\right) = \omega \sin\vartheta \sin\Phi,$$
$$\left(p_3 e_j^{(1)}\right) = -\omega_3 \sin\theta_3 \sin\varphi, \quad \left(p_4 e_j^{(1)}\right) = \omega_4 \sin\theta_4 \sin\varphi, \tag{A7}$$
$$\left(e_i^{(1)} e_j^{(1)}\right) = 1 \quad \text{and} \quad \left(e_i^{(1)} e_j^{(2)}\right) = 0 \tag{A8}$$

for any pair i, j, and

$$\left(e_i^{(2)} e_j^{(2)}\right) = 1 \quad \text{for} \quad i = j,$$
$$\left(e_1^{(2)} e_2^{(2)}\right) = \cos 2\vartheta, \left(e_3^{(2)} e_4^{(2)}\right) = \cos(\theta_3 + \theta_4) \equiv \cos\theta_+,$$
$$\left(e_1^{(2)} e_3^{(2)}\right) = \cos(\vartheta - \theta_3), \left(e_2^{(2)} e_4^{(2)}\right) = \cos(\vartheta - \theta_4),$$
$$\left(e_1^{(2)} e_4^{(2)}\right) = \cos(\vartheta + \theta_4), \left(e_2^{(2)} e_3^{(2)}\right) = \cos(\vartheta + \theta_3), \tag{A9}$$

and

$$(p_1 p_2) = \omega^2(\cos 2\vartheta - 1) = (p_3 p_4) = \omega_3\omega_4(\cos\theta_+ - 1), \tag{A10}$$

where $(p_1 + p_2)^2 = (p_3 + p_4)^2$ is required for massless photons.

We are now ready to estimate the factor $\mathcal{G}$ included in the partially integrated cross section at Eq. (A24) in Ref. [22]. We evaluate the case of $ab = 11$ for the scalar exchange. From the first of Eq. (A2), we obtain

$$\begin{aligned}\mathcal{V}_{11}^{[1]\mathrm{SC}} &= (p_1 p_2)\left(e_1^{(1)} e_2^{(1)}\right) - \left(p_1 e_2^{(1)}\right)\left(p_2 e_1^{(1)}\right) \\ &= \omega^2\left(\cos 2\vartheta - 1 + \sin^2\vartheta \sin^2\Phi\right) \sim \omega^2\vartheta^2\left(2 - \sin^2\Phi\right),\end{aligned} \tag{A11}$$

where the first of Eq. (A10), Eq. (A5), and $\left(p_1 e_2^{(1)}\right)\left(p_2 e_1^{(1)}\right) = -(\omega \sin\vartheta \sin\Phi)^2$ are substituted. The last approximation is based on $\vartheta \sim \vartheta_r \ll 1$.

This yields the following averaging factor on the incident reaction plane:

$$\mathcal{G}_{11}^{\mathrm{SC}} = \frac{\int_0^{2\pi}\left(2 - \sin^2\Phi\right)^2 d\Phi}{8\pi} = \frac{19}{32}. \tag{A12}$$

We also provide the case of $ab = 12$ for the pseudoscalar exchange as follows. Based on the first of Eq. (A3), the first vertex factor with vector definitions above is expressed as

$$\begin{aligned}\mathcal{V}_{12}^{[1]\mathrm{PS}} &= -\epsilon^{\mu\nu\rho\sigma} p_{1\mu} p_{2\rho} e_{1\nu}^{(1)} e_{2\sigma}^{(2)} = -p_{1\mu} p_{2\rho} \epsilon^{\mu y\rho\sigma} e_{2\sigma}^{(2)} \\ &= -p_{1\mu} p_{2\rho}\left[\epsilon^{\mu y\rho x}(-\cos\vartheta) + \epsilon^{\mu y\rho z}(-\sin\vartheta)\right] \\ &= p_{2\rho}\left[\left(p_{10}\epsilon^{0y\rho x} + p_{1z}\epsilon^{zy\rho x}\right)\cos\vartheta + \left(p_{10}\epsilon^{0y\rho z} + p_{1x}\epsilon^{xy\rho z}\right)\sin\vartheta\right] \\ &= p_{2\rho}\left[\left(-\omega\epsilon^{0y\rho x} + \omega\cos\vartheta\epsilon^{zy\rho x}\right)\cos\vartheta + \left(-\omega\epsilon^{0y\rho z} + \omega\sin\vartheta\cos\Phi\epsilon^{xy\rho z}\right)\sin\vartheta\right] \\ &= \left[\left(-\omega\epsilon^{0yzx} p_{2z} + \omega\cos\vartheta\epsilon^{zy0x} p_{20}\right)\cos\vartheta\right. \\ &\quad \left. + \left(-\omega\epsilon^{0yxz} p_{2x} + \omega\sin\vartheta\cos\Phi\epsilon^{xy0z} p_{20}\right)\sin\vartheta\right] \\ &= \omega^2\left[(-\cos\vartheta + \cos\vartheta)\cos\vartheta + (-\sin\vartheta - \sin\vartheta)\cos\Phi\sin\vartheta\right] = -2\omega^2\sin^2\vartheta\cos\Phi.\end{aligned} \tag{A13}$$

This yields the following averaging factor on the incident reaction plane:

$$\mathcal{G}_{12}^{\mathrm{PS}} = \frac{\int_0^{2\pi} \cos^2\varphi d\varphi}{2\pi} = \frac{1}{2}. \tag{A14}$$

Appendix B. Refinement of the weight factor $\mathcal{W}$

In Ref. [3,22], we approximated $\mathcal{W}$ as the constant $\pi/2$ for a mass region much smaller than that covered by $\Delta\theta$ as a conservative estimate. This is because we preferred simplicity of the parametrization to accuracy. However, once we need to compare the sensitivity for the higher mass region with the other search methods, the validity of the approximation applicable only to the smaller mass region must be reconsidered. In the following, we first exactly repeat the relevant part of Ref. [22] and then refine $\mathcal{W}$ as a function of the sensitive mass regions by quoting the necessary equations.

We first express the squared scattering amplitude for the case when a low-mass field is exchanged in the s-channel via a resonance state with the symbol to describe polarization combinations of initial and final states S:

$$|\mathcal{M}_S|^2 \approx (4\pi)^2 \frac{a^2}{\chi^2 + a^2}, \tag{B1}$$

where $\chi = \omega^2 - \omega_r^2$ with the resonance condition $m = 2\omega_r \sin\vartheta_r$ for a given mass m, and a is expressed as

$$a = \frac{\omega_r^2}{8\pi}\left(\frac{gm}{M}\right)^2 = \frac{m\Gamma}{2\sin^2\vartheta_r} \tag{B2}$$

with the resonance decay rate of the low-mass field

$$\Gamma = (16\pi)^{-1}\left(gM^{-1}\right)^2 m^3. \tag{B3}$$

The resonance condition is satisfied when the center-of-mass system (CMS) energy between two incident photons $E_{\mathrm{CMS}} = 2\omega\sin\vartheta$ coincides with the given mass m. At a focused geometry of an incident laser beam, however, E_{CMS} cannot be uniquely specified due to the momentum uncertainty of the incident waves. Although the incident laser energy has an intrinsic uncertainty, the momentum uncertainty or the angular uncertainty between a pair of incident photons dominates that of the incident energy. Therefore, we consider the case where only angles of incidence ϑ between randomly chosen pairs of photons are uncertain within $0 < \vartheta \leq \Delta\vartheta$ for a given focusing parameter by fixing the incident energy. The treatment for the intrinsic energy uncertainty is explained in detail in the Appendix B of Ref. [22]. We fix the laser energy ω at the optical wavelength

$$\omega_{opt}^2 = \frac{m^2}{4\vartheta_r^2} \sim 1\,\mathrm{eV}^2, \tag{B4}$$

while the resonance condition depends on the incident angle uncertainty. This gives an expression for χ as a function of ϑ:

$$\chi(\vartheta) = w_{\mathrm{opt}}^2 - w_r^2(\vartheta) = \frac{m^2}{4\vartheta_r^2} - \frac{m^2}{4\vartheta^2} = \left(1 - (\vartheta_r/\vartheta)^2\right)\omega_{\mathrm{opt}}^2, \tag{B5}$$

where

$$d\vartheta = \frac{\vartheta_r}{2\omega_{\mathrm{opt}}^2}\left(1 - \frac{\chi}{\omega_{\mathrm{opt}}^2}\right)^{-3/2} d\chi. \tag{B6}$$

We thus introduce the averaging process for the squared amplitude $\overline{|\mathcal{M}_S|^2}$ over the possible uncertainty on incident angles

$$\overline{|\mathcal{M}_S|^2} = \int_0^{\pi/2} \rho(\vartheta)|\mathcal{M}_S(\vartheta)|^2 d\vartheta, \tag{B7}$$

where $\mathcal{M}_S$ specified with a set of physical parameters m and gM^{-1} is expressed as a function of ϑ, and $\rho(\vartheta)$ is the probability distribution function as a function of the uncertainty on ϑ within an incident pulse.

We review the expression for the electric field of the Gaussian laser propagating along the z-direction in spatial coordinates (x, y, z) [26] as follows:

$$\vec{E}(x, y, z) = \vec{E}_0 \frac{w_0}{w(z)} \exp\left\{-i[kz - H(z)] - r^2\left(\frac{1}{w(z)^2} + \frac{ik}{2R(z)}\right)\right\}, \tag{B8}$$

where E_0 is the electric field amplitude, $k = 2\pi/\lambda$, $r = \sqrt{x^2 + y^2}$, w_0 is the minimum waist, which cannot be smaller than λ due to the diffraction limit, and the other definitions are as follows:

$$w(z)^2 = {w_0}^2\left(1 + \frac{z^2}{{z_R}^2}\right), \tag{B9}$$

$$R = z\left(1 + \frac{{z_R}^2}{z^2}\right), \tag{B10}$$

$$H(z) = \tan^{-1}\left(\frac{z}{z_R}\right), \tag{B11}$$

$$z_R \equiv \frac{\pi {w_0}^2}{\lambda}. \tag{B12}$$

With θ being an incident angle of a single photon in the Gaussian beam, the angular distribution $g(\theta)$ can be approximated as

$$g(\theta) \sim \frac{1}{\sqrt{2\pi}\Delta\theta} \exp\left\{-\frac{\theta^2}{2\Delta\theta^2}\right\}, \tag{B13}$$

where the incident angle uncertainty in the Gaussian beam $\Delta\theta$ is introduced within the physical range $|\theta| < \pi/2$ as

$$\Delta\theta \sim \frac{\lambda_c}{\pi w_0} = \frac{d}{2f}, \tag{B14}$$

with the wavelength of the creation laser λ_c, the beam diameter d, the focal length f, and the beam waist $w_0 = \frac{f\lambda_c}{\pi d/2}$, as illustrated in Fig. 1. For a pair of photons 1, 2, each of which follows $g(\theta)$, the incident angle between them is defined as

$$\vartheta = \tfrac{1}{2}|\theta_1 - \theta_2|. \tag{B15}$$

With the variance $\Delta\vartheta^2 = 2\left(\frac{1}{4}\Delta\theta^2\right)$, the pair angular distribution $\rho(\vartheta)$ is then approximated as

$$\rho(\vartheta) \sim \frac{2}{\sqrt{\pi}\Delta\theta} \exp\left\{-\left(\frac{\vartheta}{\Delta\theta}\right)^2\right\} \sim \frac{2}{\sqrt{\pi}\Delta\theta} \quad \text{for} \quad 0 < \vartheta < \pi/2, \tag{B16}$$

where the coefficient 2 of the amplitude is caused by limiting ϑ to the range $0 < \vartheta < \pi/2$, and $\left(\frac{\vartheta}{\Delta\theta}\right)^2 \ll 1$ is taken into account because $\Delta\theta$ in Eq. (B14) also corresponds to the upper limit by the focusing lens based on geometric optics. This distribution is consistent with the flat-top distribution applied to Refs. [3,24] apart from the coefficient.

We now re-express the average of the squared scattering amplitude as a function of $\chi \equiv a\xi$ in units of the width of the Breit–Wigner (BW) distribution a by substituting Eqs. (B1) and (B16) into Eq. (B7) with Eq. (B6):

$$\overline{|\mathcal{M}_S|^2} = \frac{(4\pi)^2}{\sqrt{\pi}\omega_{\rm opt}^2}\left(\frac{\vartheta_r}{\Delta\theta}\right) a\mathcal{W}, \tag{B17}$$

where we introduce the constant

$$\mathcal{W} \equiv \int_{-\infty}^{\frac{\omega_{\rm opt}^2}{a}\left\{1-(\vartheta_r/(\pi/2))^2\right\}} W(\xi)\,\frac{1}{\xi^2+1}d\xi \tag{B18}$$

with

$$W(\xi) \equiv \left(1-\frac{a\xi}{\omega_{\rm opt}^2}\right)^{-3/2}. \tag{B19}$$

In Eq. (B18) the weight function $W(\xi)$ is a positive and monotonic function within the integral range and the second term is the BW function with a width of unity. Note that $\overline{|\mathcal{M}_S|^2}$ is now explicitly proportional to a but not a^2. This gives the enhancement factor a compared to the case $\overline{|\mathcal{M}_S|^2} \propto a^2$ where no resonance state is contained in the integral range controlled by $\Delta\theta$ experimentally. The integrated value of the pure BW function from $\xi = -1$ to $\xi = +1$ gives $\pi/2$, while that from $\xi = -\infty$ to $\xi = +\infty$ gives π. The difference is only a factor of two. The weight function $W(\xi)$ of the kernel is almost unity for small $a\xi$, that is, when a is small enough with a small mass and a weak coupling. Therefore, we will consider only the region of $\xi \pm 1$ as a conservative estimate. By taking only this integral range, we can be released from trivial numerical modifications originating from $\xi = -\infty$ and the behavior of $W(\xi)$ at $\xi = \frac{\omega_{\rm opt}^2}{a}\left\{1-(\vartheta_r/(\pi/2))^2\right\}$ which are not essential due to the strong suppression by the BW weight.

We now refine $\mathcal{W}$ in order to apply it more accurately even to the case for $\vartheta_r/\Delta\theta \sim 1$ where, exactly speaking, the second approximation in Eq. (B16) is not valid. In this case, by using the first of Eq. (B16) with substitution of the relation between $\chi \equiv a\xi$ and ϑ expressed in Eq. (B5), Eq. (B19) is modified as follows:

$$W(\xi) \equiv \exp\left\{-\frac{(\vartheta_r/\Delta\theta)^2}{1-\frac{a}{\omega_{\rm opt}^2}\xi}\right\}\left(1-\frac{a}{\omega_{\rm opt}^2}\xi\right)^{-3/2} \sim \exp\left\{-\left(\frac{\vartheta_r}{\Delta\theta}\right)^2\right\}, \tag{B20}$$

where the last approximation is based on $a/\omega_{opt}^2 \ll 1$ with respect to the integral range $\xi \pm 1$ in Eq. (B18) for the conservative estimate. This is justified in the mass–coupling range we are interested in via the first relation in Eq. (B2), for instance, $a/\omega_{\rm opt}^2 \sim 10^{-29}$ for $m \sim 0.1\,\text{eV}$ and $g/M \sim 10^{-4}\,\text{GeV}^{-1}$. By substituting Eq. (B20) into Eq. (B18), the conservative evaluation on $\mathcal{W}$ over $\xi \pm 1$ is expressed as

$$\mathcal{W} \sim \int_{-1}^{+1} W(\xi)\,\frac{1}{\xi^2+1}d\xi \sim \frac{\pi}{2}\exp\left\{-\left(\frac{\vartheta_r}{\Delta\theta}\right)^2\right\}. \tag{B21}$$

This factor is dependent on ϑ_r, equivalently dependent on mass, especially for larger ϑ_r close to $\Delta\theta$, while it is almost $\pi/2$ for smaller ϑ_r.

References

[1] Y. Fujii and K. Maeda, *The Scalar–Tensor Theory of Gravitation* (Cambridge University Press, Cambridge, 2003).

[2] Y. Fujii and K. Homma, Prog. Theor. Phys. **126**, 531 (2011); Prog. Theor. Exp. Phys. **2014**, 089203 (2014) [erratum].
[3] K. Homma, Prog. Theor. Exp. Phys. **2012**, 04D004 (2012); **2014**, 089201 (2014) [erratum].
[4] S. Weinberg, Phys. Rev. Lett. **40**, 223 (1978).
[5] F. Wilczek, Phys. Rev. Lett. **40**, 279 (1978).
[6] R. D. Peccei and H. R. Quinn, Phys. Rev. Lett. **38**, 1440 (1977).
[7] M. P. Hertzberg, M. Tegmark, and F. Wilczek, Phys. Rev. D **78**, 083507 (2008).
[8] O. Wantz and E. P. S. Shellard, Phys. Rev. D **82**, 123508 (2010).
[9] S. Moriyama et al., Phys. Lett. B **434**, 147 (1998).
[10] Y. Inoue et al., Phys. Lett. B **536**, 18 (2002).
[11] Y. Inoue et al., Phys. Lett. B **668**, 93 (2008).
[12] K. Zioutas et al. [CAST Collaboration], Phys. Rev. Lett. **94**, 121301 (2005).
[13] S. Andriamonje et al. [CAST Collaboration], J. Cosmol. Astropart. Phys. **04**, 010 (2007).
[14] E. Arik et al. [CAST Collaboration], J. Cosmol. Astropart. Phys. **02**, 008 (2009).
[15] M. Arik et al. [CAST Collaboration], Phys. Rev. Lett. **107**, 261302 (2011).
[16] R. Cameron et al., BFRT Phys. Rev. D **47**, 3707 (1993).
[17] E. Zavattini et al. [PVLAS Collaboration], Phys. Rev. D **77**, 032006 (2008).
[18] P. Pugnat et al. [OSQAR Collaboration], Phys. Rev. D **78**, 092003 (2008).
[19] K. Ehret et al. [ALPS Collaboration], Phys. Lett. B **689**, 149 (2010).
[20] S. J. Asztalos et al. [ADMX Collaboration], Phys. Rev. D **69**, 01101 (2004).
[21] S. J. Asztalos et al. [ADMX Collaboration], Phys. Rev. Lett. **104**, 041301 (2010).
[22] K. Homma, T. Hasebe, and K. Kume, Prog. Theor. Exp. Phys. **2014**, 083C01 (2014).
[23] T. Tajima and K. Homma, Int. J. Mod. Phys. A **27**, 1230027 (2012).
[24] K. Homma, D. Habs, and T. Tajima, Appl. Phys. B **106**, 229 (2012).
[25] S. A. J. Druet and J.-P. E. Taran, Prog. Quant. Electr. **7**, 1 (1981).
[26] A. Yariv, *Optical Electronics in Modern Communications* (Oxford University Press, Oxford, 1997).
[27] F. Moulin and D. Bernard, Opt. Commun. **164**, 137 (1999).
[28] E. Lundström et al., Phys. Rev. Lett. **96**, 083602 (2006).
[29] J. Lundin et al., Phys. Rev. A **74**, 043821 (2006).
[30] D. Bernard et al., Eur. Phys. J. D **10**, 141 (2000).
[31] J. Beringer et al. [Particle Data Group], Phys. Rev. D **86**, 010001 (2012).
[32] Y. Su et al., Phys. Rev. D **50**, 3614 (1994); **51**, 3135 (1995) [erratum].
[33] E. G. Adelberger et al., Phys. Rev. Lett. **98**, 131104 (2007).
[34] D. J. Kapner et al., Phys. Rev. Lett. **98**, 021101 (2007).
[35] J. Chiaverini et al., Phys. Rev. Lett. **90**, 151101 (2003).
[36] S. J. Smullin et al., Phys. Rev. D **72**, 122001 (2005); **72**, 129901 (2005) [erratum].
[37] S. K. Lamoreaux, Phys. Rev. Lett. **78**, 5 (1997); **81**, 5475 (1998) [erratum].
[38] J. E. Kim, Phys. Rev. Lett. **43**, 103 (1979).
[39] M. A. Shifman, A. I. Vainshtein, and V. I. Zakharov, Nucl. Phys. B **166**, 493 (1980).